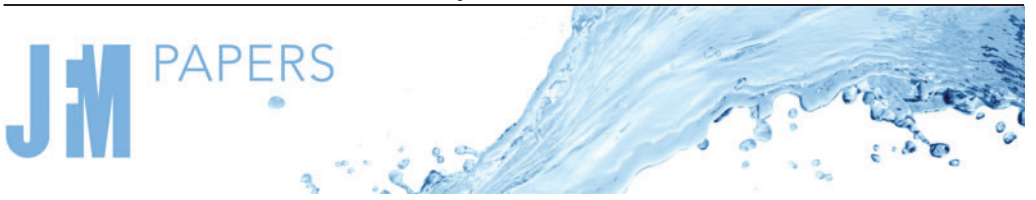
J. Fluid Mech. (2022), *vol*. 946, A28, doi:10.1017/jfm.2022.583



Surface layer response to heterogeneous tree canopy distributions: roughness regime regulates secondary flow polarity

P. Joshi[1] **and W. Anderson**[1],†

[1]Department of Mechanical Engineering, The University of Texas at Dallas, 800 West Campbell Road, Richardson, TX 75080, USA

(Received 8 February 2022; revised 23 May 2022; accepted 4 July 2022)

Large-eddy simulation was used to model turbulent atmospheric surface layer (ASL) flow over canopies composed of streamwise-aligned rows of synthetic trees of height, h, and systematically arranged to quantify the response to variable streamwise spacing, δ_1, and spanwise spacing, δ_2, between adjacent trees. The response to spanwise and streamwise heterogeneity has, indeed, been the topic of a sustained research effort: the former resulting in formation of Reynolds-averaged counter-rotating secondary cells, the latter associated with the k- and d-type response. No study has addressed the confluence of both, and results herein show secondary flow polarity reversal across 'critical' values of δ_1 and δ_2. For $\delta_2/\delta \lesssim 1$ and $\gtrsim 2$, where δ is the flow depth, the counter-rotating secondary cells are aligned such that upwelling and downwelling, respectively, occurs above the elements. The streamwise spacing δ_1 regulates this transition, with secondary cell reversal occurring first for the largest k-type cases, as elevated turbulence production within the canopy necessitates entrainment of fluid from aloft. The results are interpreted through the lens of a benchmark prognostic closure for effective aerodynamic roughness, $z_{0,Eff.} = \alpha\sigma_h$, where α is a proportionality constant and σ_h is height root mean square. We report $\alpha \approx 10^{-1}$, the value reported over many decades for a broad range of rough surfaces, for k-type cases at small δ_2, whereas the transition to d-type arrangements necessitates larger δ_2. Though preliminary, results highlight the non-trivial response to variation of streamwise and spanwise spacing.

Key words: turbulence modelling

1. Introduction

Landscape heterogeneities are intrinsically linked to locally elevated surface fluxes of momentum, heat, humidity and other quantities, including pollen and dust. Such surface

† Email address for correspondence: wca140030@utdallas.edu

© The Author(s), 2022. Published by Cambridge University Press

https://doi.org/10.1017/jfm.2022.583 Published online by Cambridge University Press

fluxes are a product of land–atmosphere interactions affecting the hydrologic cycle, whereas local heterogeneities create microclimates that profoundly alter the existence of idealised (equilibrium) atmospheric surface layer (ASL) conditions.

Horizontally homogeneous neutrally stratified ABL (Wyngaard 2010) flow over a homogeneous distribution of roughness elements is composed of a roughness sublayer and an inertial layer aloft, where the former is occupied by vortical mixing processes regulated by the spatial extent of roughness elements (Raupach, Antonia & Rajagopalan 1991; Raupach, Finnigan & Brunet 1996; Jimenez 2004; Castro 2007; Ghisalberti 2009), whereas the latter is occupied by wall-attached eddies (Townsend 1976) and large-scale motions (Hutchins & Marusic 2007). For a homogeneous distribution of elements with aggregate height, h, the roughness sublayer depth, $\lambda_{\mathcal{R}} \approx 5h$ (Grass 1971; Raupach *et al.* 1991; Harmon & Finnigan 2007). In practice, however, roughness elements are seldom distributed homogeneously across landscapes, but exhibit local heterogeneity that confounds prognostic descriptions based upon horizontally homogeneous conditions (Bou-Zeid *et al.* 2020; Stoll *et al.* 2020).

Such spatial heterogeneity is realised via distributions of, for example, buildings, topographic undulations, sand dunes, wind turbines or vegetation. For this study, we have specifically focused on spatial heterogeneity realised via distributions of virtual trees within large-eddy simulation (LES) of ASL turbulence; it is stressed, though, that virtual trees serve a more general purpose in behaving as generalised drag elements (Belcher, Jerram & Hunt 2003).

Flow over vegetation has been studied for many years (Finnigan 2000), where preceding studies have focused on aggregate canopy dynamics (Shaw & Schumann 1992; Raupach *et al.* 1996; Su *et al.* 1998), the coupled effect of canopies and topography (Belcher, Harman & Finnigan 2012), turbulence response to the multiscale nature of trees (Graham & Meneveau 2012; Bai, Katz & Meneveau 2015), flow response with variable canopy layout (Bailey & Stoll 2013) and fundamental vortical flow processes above canopies (Finnigan, Shaw & Patton 2009; Bailey *et al.* 2014; Bailey & Stoll 2016). Though by no means exhaustive, this literature survey points to the depth of prior contributions in this area. Bailey & Stoll (2013) specifically addressed the problem of ASL flow aloft sparse canopy arrangements, although in their case sparsity was realised via streamwise heterogeneity. In this work, we are specifically interested in spanwise heterogeneity and the non-trivial confluence of effects associated with variation in the streamwise and spanwise spacing between adjacent elements.

1.1. *Roughness-driven secondary flows*

In recent years, substantial new work has demonstrated the passive actuator-like influence of spanwise heterogeneity in surface texture on wall turbulence. This largely originates with Hinze (1967), who reported results of spanwise-variable surface roughness in rectangular duct flows. Hinze showed that such an arrangement induced Reynolds-averaged secondary flows, which differed from contemporaneous observations of secondary 'corner' flows (Prandtl 1952; Hoagland 1960; Brundrett & Baines 1964; Perkins 1970; Gessner 1973). These studies were foremost in establishing the role of Reynolds (turbulent) stress spatial heterogeneity in sustenance of secondary flows or turbulent secondary flow of the second kind (Bradshaw 2003). This can be appreciated via the Reynolds-averaged vorticity transport equation:

$$\frac{\mathrm{D}\langle\boldsymbol{\omega}\rangle_t}{\mathrm{D}t} = \langle\boldsymbol{\omega}\rangle_t \cdot \boldsymbol{\nabla}\langle\boldsymbol{u}\rangle_t + Re_\tau^{-1}\nabla^2\langle\boldsymbol{\omega}\rangle_t - \boldsymbol{\nabla}\times\left(\boldsymbol{\nabla}\cdot\langle\boldsymbol{u}'\otimes\boldsymbol{u}'\rangle_t\right), \tag{1.1}$$

https://doi.org/10.1017/jfm.2022.583 Published online by Cambridge University Press

where $\langle\cdot\rangle_t$ denotes time averaging of an ergodic system, $\boldsymbol{\omega} = \boldsymbol{\nabla} \times \boldsymbol{u}$ is vorticity and $\boldsymbol{u}$ is velocity, the first, second and third terms on the right-hand side denote the stretching-and-tilting term, dissipation and turbulent torque. Here $Re_\tau = u_* \delta / \nu$ is a bulk Reynolds number, where u_* is the shear velocity, δ is the flow (ASL) depth, ν is kinematic viscosity and $\langle \boldsymbol{u}' \otimes \boldsymbol{u}' \rangle_t$ is the Reynolds-averaged Reynolds (turbulent) stress tensor. Note that in this article, the first, second and third component of any vector denote magnitude in the streamwise (x), spanwise (y) and vertical direction (z), respectively; velocity and vorticity vectors have components, $\{u, v, w\}$ and $\{\omega_x, \omega_y, \omega_z\}$, respectively; averaging of sample quantity, $\theta(\boldsymbol{x})$, over dimension, a, is denoted by $\langle \theta(\boldsymbol{x}) \rangle_a$.

Prior work has determined that the spatial heterogeneity of the Reynolds stresses, so-called 'turbulent torque' or Prandtl's secondary flow of the second kind, can sustain Reynolds-averaged secondary flows in a variety of scenarios. From flows in square ducts (Bradshaw 2003, and references therein), to hydraulic flows responding to spanwise-variable gravel roughness or aquatic canopy depth (Wang & Cheng 2005; Vermaas, Uijttewaal & Hoitink 2011), to idealised channel flows over canonical spanwise-heterogeneous roughness (Anderson *et al.* 2015*a*). Other studies have reported similar results in turbulent boundary layer flows over complex roughness s(Barros & Christensen 2014; Pathikonda & Christensen 2017), spanwise-heterogeneous 'herringbone' roughness (Nugroho, Hutchins & Monty 2013; Kevin *et al.* 2017), spanwise-heterogeneous roughness derived via 'LEGO' arrangements (Vanderwel & Ganapathisubramani 2015; Medjnoun, Vanderwel & Ganapathisubramani 2018, 2020) and other canonical arrangements (Stroh *et al.* 2020).

Within this work, a longstanding issue has been consistent assignment of secondary flow polarity with respect to the topographic elements. Consider, for now, the streamwise component of (1.1) for the case of high-Re_τ channel flow (i.e. absent streamwise heterogeneity):

$$\langle v \rangle_t \frac{\partial \langle \omega_x \rangle_t}{\partial y} + \langle w \rangle_t \frac{\partial \langle \omega_x \rangle_t}{\partial z} = \frac{\partial^2}{\partial z^2} \langle v'w' \rangle_t - \frac{\partial^2}{\partial y^2} \langle v'w' \rangle_t + \frac{\partial^2}{\partial y \partial z} \left(\langle v'v' \rangle_t - \langle w'w' \rangle_t \right). \quad (1.2)$$

Some groups have found that the secondary flow polarity is such that $\langle w \rangle_t < 0$ (downwelling) above relative peaks in roughness (Willingham *et al.* 2013; Barros & Christensen 2014; Anderson *et al.* 2015*a*; Yang & Anderson 2017*a*; Awasthi & Anderson 2018), while others have persistently found that $\langle w \rangle_t > 0$ (upwelling) above the elements (Goldstein & Tuan 1998; Vanderwel & Ganapathisubramani 2015; Medjnoun *et al.* 2018, 2020). In this article, LES has been used to address this apparent disagreement, where the aforementioned virtual trees are used to systematically isolate the arrangement 'triggers' needed to activate downwelling and upwelling above high roughness regions. Results will show that the confluence of streamwise and spanwise spacing confound automatic categorisation.

This can be appreciated from figure 1, which shows the canopy attributes assessed for this article, streamwise spacing between successive trees, δ_1, and spanwise spacing between adjacent rows, δ_2, where panels (*a*) and (*b*) show canopy transects in the x–z and y–z plane, respectively. In addition, figure 1 shows the tree height, h, with all geometric arguments normalised by ASL thickness, δ; additional tree attributes (h_1, h_2, h_c and d_t) are common to all cases and quantitative values are provided in the subsequent text. There has been significant interest in the role of δ_2. Yang & Anderson (2017*b*) showed that the intensity, measured via circulation, Γ, of roughness-driven secondary flows scaled as $\Gamma \sim \delta_2^2$ for $\delta_2/\delta \lesssim 1$, and began declining for $\delta_2/\delta \gtrsim 1$. Medjnoun *et al.* (2018), also, hypothesised on a similar process with their 'significance' parameter. Yet, both antecedent

https://doi.org/10.1017/jfm.2022.583 Published online by Cambridge University Press

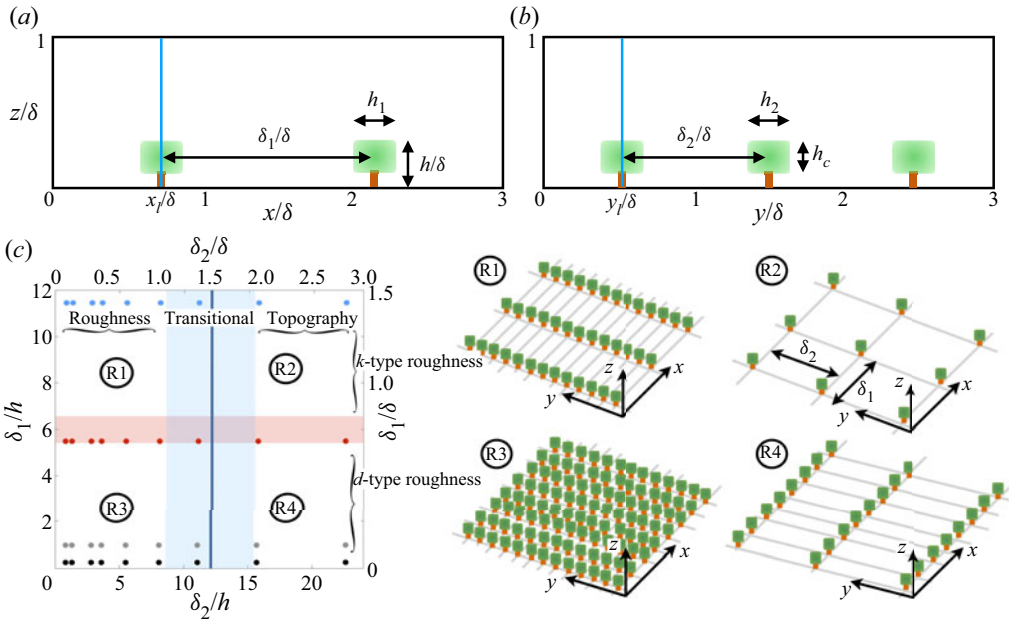


Figure 1. Schematic of tree canopy arrangements addressed as part of the research effort. Panels (*a*,*b*) show canopy visualisation in the streamwise–wall-normal and spanwise–wall-normal plane, respectively, where annotations are provided for streamwise spacing between subsequent trees, δ_1/δ, spanwise spacing between rows of trees, δ_2/δ, canopy height, h/δ, and the streamwise, spanwise and vertical extent of individual tree canopy, h_1, h_2 and h_c, respectively. Table 1 summarises specific cases; tree 'trunks' are modelled as square with side length, d_t. Panel (*c*) shows the δ_1–δ_2 parameter space (normalised by h and δ), with annotations superimposed for flow-roughness regimes predicated upon δ_1 (*k*- or *d*-type roughness) (Jimenez 2004) and δ_2 (roughness, transitional and topography regimes) (Yang & Anderson 2017*b*). In panel (*c*), filled symbols indicate the location within δ_1–δ_2 parameter space corresponding to individual cases, where *d*-type cases, intermediate cases and *k*-type cases are denoted via filled black and grey circles, filled red circles and filled blue circles, respectively (see main text). Shown also are regimes R1, R2, R3 and R4, with accompanying sketches for each regime depicted on the right, for context.

studies report differing secondary flow direction relative to the high-roughness regions. Results presented herein show that streamwise spacing between elements, δ_1, drives a reversal in the secondary flow direction. These arguments are summarised in figure 1(*c*) δ_1–δ_2 parameter space, where δ_2 is placed on the abscissa. In this panel, for context, we have superimposed annotations for the roughness, transitional and topography regimes, where the top and bottom abscissa show δ_2 normalised by flow depth and canopy height, respectively.

The dynamical significance of δ_2 can be appreciated from prior work: for $\delta_2/\delta \lesssim 1.5$, the spanwise regions between adjacent rows is inadequate to enable coexisting δ-scale secondary cells. In this case, secondary cells emanating from the roughness elements dominate, resulting in persistent upwelling above the elements. In contrast, for $\delta_2/\delta \gtrsim 1.5$, there exists sufficient spanwise spacing for two adjacent, roughness-driven, δ-scale secondary flows to coexist. This has been graphically depicted in figure 1(*c*), where regions R1/R3 and R2/R4 correspond with 'roughness' and 'topography' arrangements, which are graphically illustrated on the right. These illustrative panels highlight the relatively small and larger spanwise spacing. However, prior work in this area has failed to consider dynamical implications of streamwise spacing between streamwise-aligned topographic

https://doi.org/10.1017/jfm.2022.583 Published online by Cambridge University Press

elements, δ_1, and yet this parameter is itself a significant roughness parameter (Jimenez 2004; Flack, Schultz & Connelly 2007; Flack & Schultz 2010; Yang *et al.* 2016).

1.2. *k- and d-type roughness*

Prior research has shown that the spatial distribution of roughness elements has major implications for instantaneous and Reynolds-averaged flow response. Here, δ_1 has been shown to regulate the flow response (Perry, Schofield & Joubert 1969; Macdonald, Griffiths & Hall 1998), where for $\delta_1/h \lesssim 5$ and $\delta_1/h \gtrsim 5$ the flow response is defined as *d*- and *k*-type, respectively (see also the reviews by Raupach *et al.* (1991), Jimenez (2004), Chung *et al.* (2021) and references therein). The distinction between these roughness regimes is predicated upon flow response: for the *d*-type regime, canopy voids are occupied by *h*-scale vortices and the aloft flow 'skims' across the roughness (Macdonald *et al.* 1998); for *k*-type regime, the relatively larger intra-canopy voids provide sufficient spatial extent for separation of *h*-scale vortices. Herein, it will be shown that longstanding concerns regarding direction of roughness-driven secondary flows can be attributed to δ_1/h.

The confluence of δ_1 and δ_2 can be further appreciated from figure 1(*c*), where δ_1 is shown on the ordinate (normalised by h and δ at left and right, respectively). The transition from *d*- to *k*-type, itself not a fixed quantity, is highlighted via the superimposed transparent red band at $\delta_1/h \approx 6$. With this, we see the emergence of regimes R1 to R4, based upon topography attributes within the δ_1–δ_2 parameter space. It is apparent that regimes R3 and R2 correspond with dense and sparse arrangements, respectively, whereas regimes R1 and R4 manifest as spanwise and streamwise ridges, respectively, where the former will induce internal boundary layer (IBL) formation (Antonia & Luxton 1971; Bou-Zeid, Meneveau & Parlange 2005) and the latter will sustain Reynolds-averaged counter-rotating secondary cells (Anderson *et al.* 2015*a*).

It is self-evident that distinct response modalities, from IBL (regime R1) to streamwise secondary cells (regime R4), will collapse for case with $\delta_1/h \approx 6$ and $\delta_2/\delta \approx 1.5$. In this study, topographic arrangements were designed precisely for the purpose of targeting these cases, as will be outlined in the following developments. Results will show that secondary flow polarity is consistent with prior work, but that δ_1/h regulates the δ_2 threshold at which polarity is reversed.

1.3. *This study*

We have used LES to conduct an extensive parametric study on the influence of δ_1 and δ_2 for roughness-driven secondary flows. Results will show that, as per prior studies, secondary flow intensity strengthens with increasing spanwise spacing, δ_2. This is recorded via circulation in the spanwise–wall-normal plane, as per prior studies (Yang & Anderson 2017*b*; Anderson *et al.* 2018; Anderson 2019). Likewise, it will be shown that downwelling and upwelling occurs above the elements for distinct 'topography' and 'roughness' regime cases, irrespective of the *k*- or *d*-type configuration. We, however, show that the transition to downwelling, i.e. secondary flow polarity reversal, occurs first for the largest δ_1/h.

Although virtual trees are used as drag elements, these can be interpreted as general wall-mounted obstacles, which play the role of absorbing momentum fluxes (i.e. conceptual scientific deductions realised from the work are not expected to differ if the work were repeated with, for example, cubes instead of virtual trees) (Ghisalberti 2009). In § 2.1, details of the LES code and computational cases are presented. Results are presented

https://doi.org/10.1017/jfm.2022.583 Published online by Cambridge University Press

in § 3, and concluding remarks are presented in § 4. In the Appendix, results of LES modelling of flow over canopies considered in a prior article are presented (Bailey & Stoll 2013), to demonstrate efficacy of the present simulations.

2. Numerical methodology and cases

2.1. *LES code*

The spatially filtered incompressible momentum transport equation is solved, $\mathrm{D}_t\tilde{\boldsymbol{u}}(\boldsymbol{x}, t) = \boldsymbol{f}(\boldsymbol{x}, t)$, where the grid-filtering operation is performed via convolution with the filtering kernel, $\tilde{\boldsymbol{u}}(\boldsymbol{x}, t) = G_\Delta \star \boldsymbol{u}(\boldsymbol{x}, t)$, where $\widetilde{\ldots}$ denotes a grid-filtered quantity. $\boldsymbol{f} = -\rho^{-1}\boldsymbol{\nabla} p - \boldsymbol{\nabla}\cdot\boldsymbol{\tau} + \boldsymbol{e}_1\Pi + \boldsymbol{f}_b$, where ρ is density, $\boldsymbol{\nabla} p$ is a pressure correction required to preserve a divergence-free (incompressible) flow, $\boldsymbol{\nabla}\cdot\tilde{\boldsymbol{u}} = 0$, $\boldsymbol{\tau} = \widetilde{\boldsymbol{u}'\otimes\boldsymbol{u}'}$ is the subgrid-scale stress tensor, where $\boldsymbol{u}' = \boldsymbol{u} - \tilde{\boldsymbol{u}}$, $\Pi = \rho^{-1}\,\mathrm{d}P_0/\,\mathrm{d}x$ is an imposed pressure gradient and $\boldsymbol{f}_b$ is a body force used to represent the presence of virtual trees within the computational mesh (discussion to follow). Note that the shear-normalised viscous stress tensor, $Re_\tau^{-1}\nabla^2\tilde{\boldsymbol{u}}$, is omitted because $Re_\tau = u_*\delta\nu^{-1} \sim O(10^7)$ for the inertia-dominated (fully rough) flow conditions typical of geophysical/engineering wall-sheared turbulence, where u_* is the shear velocity, δ is flow depth (channel half-height) and ν is kinematic viscosity. A solenoidal velocity field is maintained by computing the divergence of the momentum transport equation, $\mathrm{D}_t[\boldsymbol{\nabla}\cdot\tilde{\boldsymbol{u}}(\boldsymbol{x}, t)] = \boldsymbol{\nabla}\cdot\boldsymbol{f}(\boldsymbol{x}, t)$, applying the divergence-free condition, $\boldsymbol{\nabla}\cdot\tilde{\boldsymbol{u}} = 0$ and solving the resultant pressure Poisson equation with Neumann conditions at the domain top and bottom, $\partial\tilde{p}/\partial z|_{z/\delta=1} = 0$ and $\partial\tilde{p}/\partial z|_{z/\delta=0} = 0$, respectively. Spectral discretisation is used in the horizontal directions, whereas vertical gradients are evaluated with centred second-order finite differencing. The domain centreline conditions are imposed with zero wall-normal gradients of streamwise and spanwise velocity and zero vertical velocity. Owing to horizontal spectral discretisation, periodic boundary conditions are imposed on the vertical 'walls' of the domain. In this sense, the numerical procedure replicates the periodic half-channel, a benchmark flow configuration (Stevens, Wilczek & Meneveau 2014). The turbulent half-channel replicates high-Rossby-number, neutrally stratified atmospheric boundary layer; channel centreline conditions capture the influence of the aloft capping inversion (Wyngaard 2010).

The deviatoric component of the subgrid-scale stresses, $\boldsymbol{\tau}^d$, is evaluated using the eddy viscosity modelling approach, $\boldsymbol{\tau}^d = \boldsymbol{\tau} - \frac{1}{3}\boldsymbol{\delta}:\boldsymbol{\tau} = -2\nu_t\tilde{\boldsymbol{S}}$, where $\nu_t = (C_s\Delta)^2|\tilde{\boldsymbol{S}}|$ is the turbulent viscosity, C_s is the Smagorinsky coefficient, Δ is the filter size, $\tilde{\boldsymbol{S}} = (\partial\tilde{\boldsymbol{u}} + \partial\tilde{\boldsymbol{u}}^{\mathrm{T}})/2$ is the resolved strain-rate tensor and $|\tilde{\boldsymbol{S}}| = (2\tilde{\boldsymbol{S}}{:}\tilde{\boldsymbol{S}})^{1/2}$ is the magnitude of the resolved strain-rate tensor. In the present study, C_s is evaluated dynamically during LES with the Lagrangian scale-dependent dynamic subgrid-scale model of Bou-Zeid *et al.* (2005). The present LES code has been used in many studies of inertia-dominated, rough-wall turbulence (Anderson *et al.* 2015*a*, and references therein).

The computational mesh is discretised via $\Delta_x = L_x/N_x$, $\Delta_y = L_y/N_y$ and $\Delta_z = L_z/N_z$, where $\{L_x, L_y, L_z\}$ is the domain spatial extent and $\{N_x, N_y, N_z\}$ is grid resolution; computational domain spatial extent and computational resolution details to follow. The lower wall momentum fluxes are modelled with a hybrid approach to numerically represent the presence of canopy trees affixed to a lower wall. For the wall itself, surface stress is modelled under logarithmic (equilibrium) conditions with baseline roughness length, $\hat{z}_0/\delta = 2.5\times10^{-3}$ (Anderson & Meneveau 2010*a*). This work is, thus, entirely predicated upon local (space–time) efficacy of the logarithmic law (i.e. the presumption of local space–time equilibrium conditions in a complex flow). In the strictest possible sense,

https://doi.org/10.1017/jfm.2022.583 Published online by Cambridge University Press

local equilibrium never exists, but in recent years there has been widespread use of the logarithmic law in such conditions. Bou-Zeid *et al.* (2005) demonstrated that such use of the logarithmic law could be successful in channel flows, and many immersed boundary methods leverage the logarithmic law for prescription of peripheral stresses (Graham & Meneveau 2012, and references therein). Note that results for comparison against a benchmark literature dataset are shown in the Appendix (Bailey & Stoll 2013). All flow statistics are normalised by a computational shear velocity, u_*, which is necessarily derived *a posteriori* for the canopy cases as $u_*^2 = \max\langle|\tilde{u}'\tilde{w}'|\rangle_t(\boldsymbol{x}) + \max\langle|\tau_{xz}|\rangle_t(\boldsymbol{x})$ (Bailey & Stoll 2013); this maximum value provides the correct normalising velocity scale against which turbulence statistics can be normalised, thereby enabling dynamic similarity for correct comparison of cases.

To resolve the actual trees, we use a canopy drag model (Brown, Hobson & Wood 2001; Graham & Meneveau 2012; Bailey & Stoll 2013):

$$\boldsymbol{f}_b(\boldsymbol{x}, t) = C_d a(\boldsymbol{x})\tilde{\boldsymbol{u}}(\boldsymbol{x}, t)U(\boldsymbol{x}), \tag{2.1}$$

where C_d is the drag coefficient, set to unity in this work to reflect the fully rough (inertia-dominated) flow conditions (Jimenez 2004; Anderson & Meneveau 2010*b*; Anderson 2012), $a(\boldsymbol{x})$ is the leaf-area density, which varies in space due to spatial heterogeneity of the canopy, and $U(\boldsymbol{x}) = (\langle\tilde{\boldsymbol{u}}(\boldsymbol{x}, t)\rangle_t : \langle\tilde{\boldsymbol{u}}(\boldsymbol{x}, t)\rangle_t)^{1/2}$ is the scalar wind speed. In order to compare the cases addressed herein, we have summarised the leaf-area index (LAI) (Finnigan 2000; Bailey & Stoll 2013):

$$\lambda = \int_{d^3\boldsymbol{x}} a(\boldsymbol{x})\,\mathrm{d}^3\boldsymbol{x}. \tag{2.2}$$

2.2. *Vegetation canopies*

In order to address the role of canopy element distributions, we assembled the cases summarised in table 1. We systematically address the role of δ_1 and δ_2 by fixing the former and varying the latter over targeted values known to encompass critical values of the parameter space. Figure 1 is a schematic of synthetic canopy arrangements, and provides graphical depiction of δ_1 and δ_2. We quantify flow response to spanwise heterogeneity (δ_2) for k- and d-type roughness (δ_1). Given the large number of cases, we define table 1 case names via concatenation of three symbols:

$$\text{Case} \equiv \underbrace{(\text{Symbol 1})}_{\substack{\text{Roughness}\\ k \text{ or } d\text{−type}}} \quad \underbrace{(\text{Symbol 2})}_{\substack{\text{Streamwise spacing},\delta_1\\ 1 \text{ to } 4}} \quad \underbrace{(\text{Symbol 3})}_{\substack{\text{Spanwise spacing},\delta_2\\ 1 \text{ to } 9}}. \tag{2.3}$$

The underbrace text summarises the parameter corresponding with each symbol. For these cases, we report λ and $\langle a(\boldsymbol{x})\rangle_{xyz}$ in table 1. For all cases, the streamwise, spanwise and vertical extent of trees canopies is $h_1/\delta = 0.03125$, $h_2/\delta = 0.03125$ and $h_c/\delta = 0.075$, respectively, whereas the tree 'trunks' are squares with side length, $d_t/\delta = 0.0156$. For the cases considered, with $\delta/h = 8$, the large elements induce vortical motions that precludes assumption of outer-layer similarity (Townsend 1976). Turbulence statistics shown in the following section attenuate monotonically towards the domain centreline, indicating adequate resolution and no unphysical numerical effects associated with the prescribed boundary conditions. In table 1, $z_{0,Eff.}/\delta$ and $\langle(h')^2\rangle_{xy}^{1/2}/\delta$ denote effective roughness length and root mean square (r.m.s.) of the height distribution, respectively, where $h' = h - \langle h\rangle_{xy}$.

https://doi.org/10.1017/jfm.2022.583 Published online by Cambridge University Press

Case	$\frac{\delta_1}{h}$	$\frac{\delta_2}{h}$	$\frac{\delta_1}{\delta}$	$\frac{\delta_2}{\delta}$	$\frac{z_{0,Eff.}}{\delta}$	$\frac{\langle (h')^2 \rangle_{xy}^{1/2}}{\delta}$	λ	$\langle a(\boldsymbol{x}) \rangle_{xyz}$	$\frac{L_x}{\delta}$	$\frac{L_y}{\delta}$
$d11$	0.25	1.25	0.03125	0.156	5.6×10^{-4}	3.3×10^{-2}	4.7×10^{-2}	4.2×10^{-2}	3	3
$d12$	0.25	1.75	0.03125	0.219	4.4×10^{-4}	2.9×10^{-2}	3.5×10^{-2}	3.1×10^{-2}	3	3
$d13$	0.25	2.75	0.03125	0.344	2.8×10^{-4}	2.4×10^{-2}	2.3×10^{-2}	2.1×10^{-2}	3	3
$d14$	0.25	3.75	0.03125	0.469	1.9×10^{-4}	2.1×10^{-2}	1.8×10^{-2}	1.6×10^{-2}	3	3
$d15$	0.25	5.75	0.03125	0.719	1.1×10^{-4}	1.8×10^{-2}	1.2×10^{-2}	1.0×10^{-2}	3	3
$d16$	0.25	7.75	0.03125	0.969	7.5×10^{-5}	1.5×10^{-2}	8.8×10^{-3}	7.8×10^{-3}	3	3
$d17$	0.25	11.75	0.03125	1.469	5.0×10^{-5}	1.3×10^{-2}	5.8×10^{-3}	5.2×10^{-3}	3	3
$d18$	0.33	15.75	0.04160	1.969	5.6×10^{-5}	9.5×10^{-3}	4.4×10^{-3}	3.9×10^{-3}	3	4
$d19$	0.50	23.75	0.06250	2.969	6.9×10^{-5}	6.3×10^{-3}	2.9×10^{-3}	2.6×10^{-3}	3	6
$d21$	1	1.25	0.125	0.156	3.3×10^{-4}	2.8×10^{-2}	1.9×10^{-2}	1.7×10^{-2}	3	3
$d22$	1	1.75	0.125	0.219	2.6×10^{-4}	2.4×10^{-2}	1.4×10^{-2}	1.3×10^{-2}	3	3
$d23$	1	2.75	0.125	0.344	1.6×10^{-4}	2.0×10^{-2}	9.6×10^{-3}	8.6×10^{-3}	3	3
$d24$	1	3.75	0.125	0.469	1.3×10^{-4}	1.8×10^{-2}	7.2×10^{-3}	6.5×10^{-3}	3	3
$d25$	1	5.75	0.125	0.719	7.5×10^{-5}	1.5×10^{-2}	4.8×10^{-3}	4.3×10^{-3}	3	3
$d26$	1	7.75	0.125	0.969	5.0×10^{-5}	1.2×10^{-2}	3.6×10^{-3}	3.3×10^{-3}	3	3
$d27$	1	11.75	0.125	1.469	4.4×10^{-5}	1.0×10^{-2}	2.4×10^{-3}	2.2×10^{-3}	3	3
$d28$	1	15.75	0.166	1.969	4.7×10^{-5}	7.7×10^{-3}	1.8×10^{-3}	1.6×10^{-3}	3	4
$d29$	1	23.75	0.25	2.969	5.6×10^{-5}	5.2×10^{-3}	1.2×10^{-3}	1.1×10^{-3}	3	6
$k31$	5.75	1.25	0.72	0.156	6.3×10^{-5}	1.0×10^{-2}	4.7×10^{-3}	4.3×10^{-3}	3	3
$k32$	5.75	1.75	0.72	0.219	5.0×10^{-5}	9.0×10^{-3}	3.5×10^{-3}	3.3×10^{-3}	3	3
$k33$	5.75	2.75	0.72	0.344	3.7×10^{-5}	7.3×10^{-3}	2.3×10^{-3}	2.2×10^{-3}	3	3
$k34$	5.75	3.75	0.72	0.469	3.4×10^{-5}	6.4×10^{-3}	1.7×10^{-3}	1.6×10^{-3}	3	3
$k35$	5.75	5.75	0.72	0.719	3.1×10^{-5}	5.3×10^{-3}	1.2×10^{-3}	1.1×10^{-3}	3	3
$k36$	5.75	7.75	0.72	0.969	2.6×10^{-5}	4.5×10^{-3}	8.7×10^{-4}	8.1×10^{-4}	3	3
$k37$	5.75	11.75	0.72	1.469	2.5×10^{-5}	3.7×10^{-3}	5.8×10^{-4}	5.4×10^{-4}	3	3
$k38$	5.75	15.75	0.72	1.969	3.2×10^{-5}	2.8×10^{-3}	4.4×10^{-4}	4.1×10^{-4}	3	4
$k39$	5.75	23.75	0.72	2.969	4.5×10^{-5}	1.9×10^{-3}	2.9×10^{-4}	2.7×10^{-4}	3	6
$k41$	11.75	1.25	1.469	0.156	4.0×10^{-5}	7.3×10^{-3}	2.7×10^{-3}	2.6×10^{-3}	3	3
$k42$	11.75	1.75	1.469	0.219	3.3×10^{-5}	6.4×10^{-3}	2.0×10^{-3}	1.9×10^{-3}	3	3
$k43$	11.75	2.75	1.469	0.344	2.9×10^{-5}	5.2×10^{-3}	1.3×10^{-3}	1.3×10^{-3}	3	3
$k44$	11.75	3.75	1.469	0.469	2.6×10^{-5}	4.5×10^{-3}	1.0×10^{-3}	9.7×10^{-4}	3	3
$k45$	11.75	5.75	1.469	0.719	2.4×10^{-5}	3.7×10^{-3}	6.7×10^{-4}	6.5×10^{-4}	3	3
$k46$	11.75	7.75	1.469	0.969	2.3×10^{-5}	3.2×10^{-3}	5.0×10^{-4}	4.9×10^{-4}	3	3
$k47$	11.75	11.75	1.469	1.469	2.3×10^{-5}	2.6×10^{-3}	3.4×10^{-4}	3.2×10^{-4}	3	3
$k48$	11.75	15.75	1.469	1.969	2.9×10^{-5}	1.9×10^{-3}	2.5×10^{-4}	2.4×10^{-4}	3	4
$k49$	11.75	23.75	1.469	2.969	3.9×10^{-5}	1.3×10^{-3}	1.7×10^{-4}	1.6×10^{-4}	3	6
R1.6	3	0.125	0.375	0.0156	2.6×10^{-5}	2.5×10^{-2}	9.3×10^{-2}	8.3×10^{-2}	3	3
R3.1	0.5	0.125	0.0625	0.0156	3.4×10^{-5}	4.7×10^{-2}	5.6×10^{-1}	4.9×10^{-1}	3	3
R3.6	3	0.125	0.375	0.0156	3.0×10^{-5}	2.5×10^{-2}	1.4×10^{-1}	1.2×10^{-1}	3	3

Table 1. Summary of vegetation canopy attributes and computational domain attributes considered for this article, where $\delta = 16\,\mathrm{m}$ for all cases. These cases will be referenced via the (2.3) symbol key. See also figure 1 for graphical depictions of streamwise and spanwise heterogeneity.

Figure 2 shows vertical profiles of canopy geometric attributes for all cases summarised in table 1 (with the exception of the comparison cases). Figure 2(*a–d*) shows vertical profiles of plane-averaged LAI, $\langle \alpha(\boldsymbol{x}) \rangle_{xy}(z)$, for cases $k1i$ (*a*), $k2i$ (*b*), $d3i$ (*c*) and $d4i$ (*d*). In these panels, the direction of decreasing δ_1 is shown, where it is apparent that leaf-area density monotonically increases as spanwise spacing declines. This is physically interpreted as relatively larger spatial volumes occupied by vegetation. In contrast, from panels (*a*) to (*d*) $\langle \alpha(\boldsymbol{x}) \rangle_{xy}(z)$ monotonically declines, owing to the relatively smaller spatial volumes occupied by vegetation. Figure 2(*e*) shows $\langle \alpha(\boldsymbol{x}) \rangle_x(y_l, z)$, where y_l is coincident

https://doi.org/10.1017/jfm.2022.583 Published online by Cambridge University Press

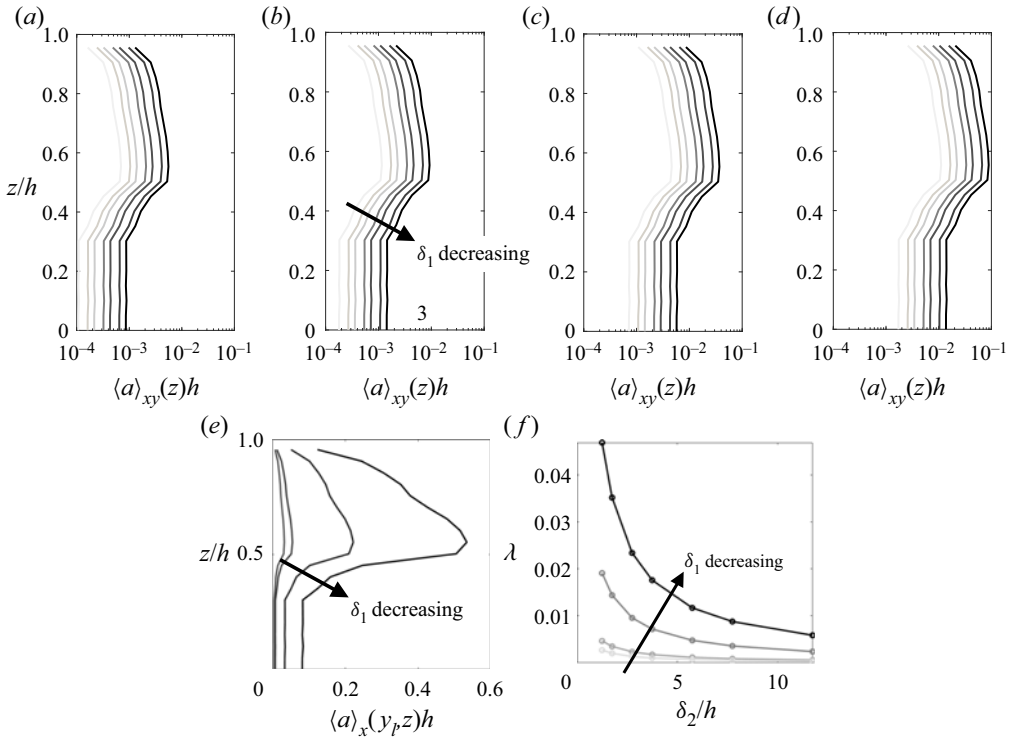


Figure 2. Vertical profiles of canopy geometric attributes for cases considered in this study. Panels (*a–d*) show vertical profiles of plane-averaged leaf-area density averaged for cases *k*1*i* (*a*), *k*2*i* (*b*), *d*3*i* (*c*) and *d*4*i* (*d*), where index *i* varies between 1 and 9 for variable δ_2 (see also table 1 and (2.3)), and where an annotation for the direction of decreasing δ_1 has been superimposed for perspective. Panel (*e*) shows streamwise-averaged leaf-area density at spanwise location, y_l, coincident with the centre of a row of trees, where an annotation for direction of δ_1 is provided. Panel (*f*) shows the LAI, λ (2.2), for all table 1 cases (with the exception of the comparison cases), with the direction of decreasing δ_1 indicated.

with the centre of a streamwise-aligned row of trees (given the sampling at y_l, panel (*e*) is insensitive to spanwise spacing and captures only variability in δ_1). Finally, figure 2(*f*) shows the LAI, λ, for all cases in table 1 (with the exception of the comparison cases). Each datapoint on panel (*f*) corresponds with a case, and solid lines are used to 'group' cases with fixed δ_1. These graphical illustrations of canopy geometric attributes are helpful in demonstrating consistent, monotonic trends with variation in δ_1 and δ_2 (see also figure 1 and (2.3) for canopy schematic and case code equation, respectively).

In order to demonstrate efficacy of the present LES code, we have also modelled ASL flow over cases R1.6, R3.1 and R3.6, with attributes summarised in table 1. These cases are identical to those already considered by Bailey & Stoll (2013). Comparison of results from the present LES code against those reported previously by an independent group help to establish efficacy of the numerical approach; comparison results are shown in the Appendix. It is also noted that the LES code has now been in use for several decades and has been successfully used in a variety of research avenues.

For all cases, we used $L_x/\delta = 3$ and $L_z/\delta = 1$, with $\delta/h = 8$; L_y/δ was varied to accommodate the canopy attributes, as recorded in table 1. This value of δ/h is sufficient to ensure that the flow is dominated by roughness sublayer dynamics, with no capacity for large-scale correlation in the outer layer (Raupach *et al.* 1991, 1996; Ghisalberti 2009;

https://doi.org/10.1017/jfm.2022.583 Published online by Cambridge University Press

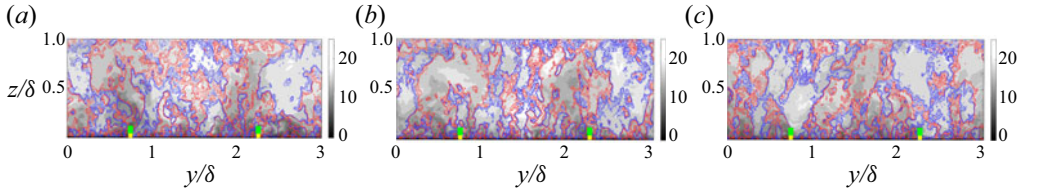


Figure 3. Contours of instantaneous streamwise velocity in the y–z plane at $x = L_x/2$, with isocontours of vertical velocity superimposed for values, $\tilde{w}(\boldsymbol{x}, t)/u_* = 1$ (red) and -1 (blue). Results are shown for table 1 cases with $\delta_2/\delta = 1.5$ and $\delta_1/h = 0.25$ ($d17$, panel a), $\delta_1/h = 5.75$ ($k37$, panel b) and $\delta_1/h = 11.75$ ($k47$, panel c). Canopy elements are denoted with green silhouettes.

Anderson, Li & Bou-Zeid 2015*b*). For this reason, the domain streamwise extent imposes no unphysical truncation of energy-containing large-scale motions, because roughness sublayer processes preclude emergence of outer-layer correlation (Hutchins & Marusic 2007). The computational domain is discretised with $\{N_x, N_y, N_z\} = \{192, 192, 160\}$, which is consistent with Bailey & Stoll (2013).

3. Results

A series of results are presented to address the underlying question on secondary flow polarity in high-Reynolds-number channel flows over spanwise- and streamwise-heterogeneous canopies. As noted in § 1.1, this issue has been the topic of a sustained research effort regarding the polarity of roughness-driven secondary flows; that is, contrasting the results from Ganapathisubramani and coworkers (Vanderwel & Ganapathisubramani 2015; Medjnoun *et al.* 2018, 2020) against those from Anderson, Christensen, and others (Willingham *et al.* 2013; Barros & Christensen 2014; Anderson *et al.* 2015*a*; Pathikonda & Christensen 2017; Yang & Anderson 2017*a*; Awasthi & Anderson 2018; Zheng & Anderson 2021). Results will demonstrate that, indeed, k- or d-type roughness can regulate the polarity of roughness-driven secondary flows, where the former and latter induce upwelling and downwelling aloft streamwise-aligned roughness 'rows', respectively. This ability to regulate polarity is pronounced only in the transitional zone (based on δ_2).

In order to efficiently present flow visualisations, we show instantaneous and Reynolds-averaged flow visualisations for cases spanning the transitional regime with respect to δ_2 and the d- and k-type regimes; indeed, the cases were designed *a priori* for precisely this reason. Results are shown in the spanwise–wall-normal plane, to illustrate large-scale flow response. Figures 3 and 4 show instantaneous and time-averaged results, respectively, for cases noted in the caption.

For case $d17$, with the lowest δ_1/h, streamwise spacing between successive elements is $\delta_1/h = 0.25$, the flow is expected to 'skim' over successive elements in a manner that precludes intra-canopy flow reattachment (Macdonald *et al.* 1998; Jimenez 2004) (figure 3*a*). In contrast, the corresponding spanwise spacing, $\delta_2/\delta = 1.5$, is in the transitional regime (figure 1*c* and accompanying text). For case $d17$, figure 3(*a*) shows the large-scale fluctuation typical of instantaneous visualisation. Note, however, pronounced regions of relative streamwise momentum deficit and corresponding upwelling (red). This modality is also observed for case $k37$, which is in the d- to k-type transition region. The structure observed in figure 3(*a*,*b*), though based only on instantaneous visualisation, is consistent with results from Ganapathisubramani and coworkers (Vanderwel & Ganapathisubramani 2015; Medjnoun *et al.* 2018, 2020). However, for case $k47$ (figure 3*c*),

https://doi.org/10.1017/jfm.2022.583 Published online by Cambridge University Press

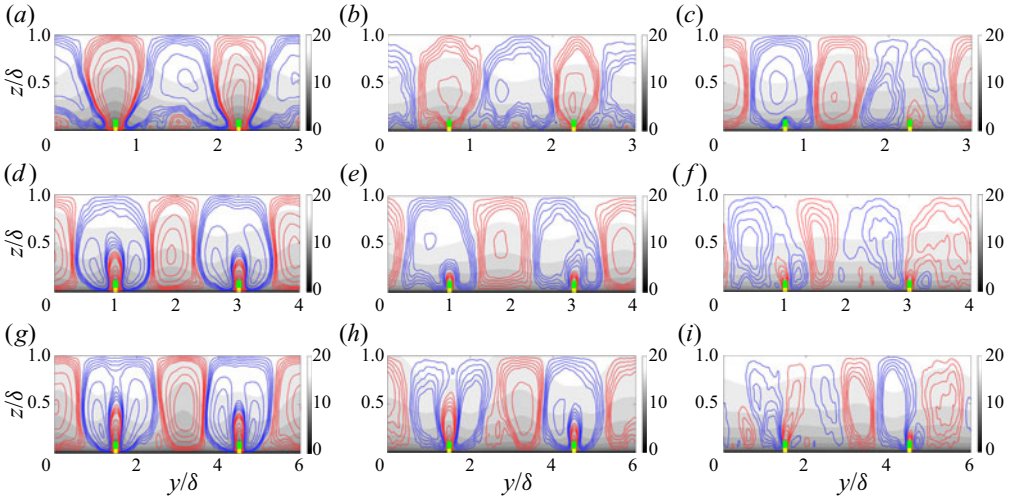


Figure 4. Contours of Reynolds-averaged streamwise velocity in the y–z plane at $x = L_x/2$, with isocontours of vertical velocity superimposed for values, $\langle\tilde{w}\rangle_t(\boldsymbol{x})/u_* = 1$ (red) and -1 (blue). Results are shown for table 1 cases with $\delta_2/\delta = 1.5$ (*a–c* show results for cases *d*17, *k*37 and *k*47), 2 (*d–f* show results for cases *d*18, *k*38 and *k*48) and 3 (*g–i* show results for cases *d*19, *k*39 and *k*49) and streamwise spacing $\delta_1/h = 0.25$ (*a*,*d*,*g*), 5.75 (*b*,*e*,*h*) and 11.75 (*c*,*f*,*i*). Canopy elements are denoted with green silhouettes.

for which $\delta_1/h = 11.75$ and the elements are thoroughly within the *k*-type regime, regions of aggregate momentum excess reside aloft the row of trees, a polarity reversal from the observations presented in figure 3(*a*,*b*).

Figure 4 provides further insight on secondary flow structure via Reynolds-averaged results. The top, middle and bottom row of panels corresponds with $\delta_2/\delta = 1.5$, 2 and 3, respectively, whereas the left, middle and right column correspond with $\delta_1/h = 0.25$, 5.75 and 11.75, respectively. For the clear *d*-type cases (panels *a*,*d*,*g*), note that upwelling occurs only for $\delta_2/\delta = 1.5$ (panel *a*); for cases with relatively larger δ_2/δ, i.e. clearly within the topography regime, downwelling is observed above the panels, with upwelling concentrated only in the roughness sublayer region of the elements.

For cases with intermediate streamwise heterogeneity (*k*37, *k*38 and *k*39, shown in figure 4*b*, *e* and *h*, respectively), upwelling is observed only for the case with the smallest spanwise heterogeneity (panel *b*). For cases with relatively larger spanwise heterogeneity, upwelling is concentrated within the roughness sublayer, but this is encompassed within a region of downwelling. Note also that for case *k*37, the domain-scale upwelling corresponds with a region of relative streamwise momentum deficit, whereas for cases *k*38 and *k*39, downwelling corresponds with a relative streamwise momentum excess. The latter modality represents a high-momentum pathway (HMP), as per Christensen and colleagues (Barros & Christensen 2014), whereas the former is consistent with findings from Ganapathisubramani and coworkers (Vanderwel & Ganapathisubramani 2015; Medjnoun *et al.* 2018, 2020). This result illustrates the significant extent to which both streamwise and spanwise heterogeneity regulate secondary flow modality.

For the very largest streamwise heterogeneity (figure 4*c*,*f*,*i*), downwelling occurs above the roughness elements for all cases: this can be appreciated by coincident downwelling and relative streamwise momentum excess. Based only upon figure 4, a relative demarcation in secondary flow modality could be envisioned between cases *d*17 and *k*37 above and those below. As the results discussion advances, we show that both modalities

https://doi.org/10.1017/jfm.2022.583 Published online by Cambridge University Press

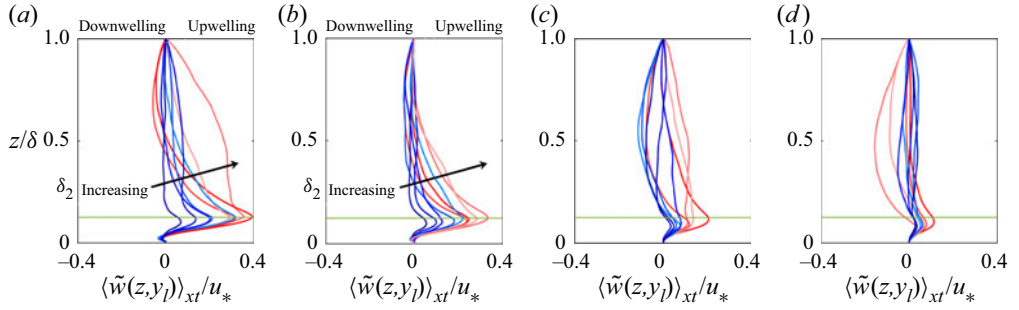


Figure 5. Vertical profiles of x- and Reynolds-averaged vertical velocity at spanwise location, y_l, coincident with the centre of a row of trees. Panels (a–d) show results for cases $d1i$, $d2i$, $k3i$ and $k4i$, respectively, where $i = 1$–9 corresponds with a colour transition from red to blue. Annotations superimposed for downwelling and upwelling. The canopy elevation, h/δ, is denoted by horizontal green lines, and the direction of increasing δ_2 is shown for perspective.

are a manifestation of the same underlying flow physics: relative spatial imbalances of production and dissipation of turbulent kinetic energy, $tke(\boldsymbol{x}) = (1/2)(\langle\tilde{\boldsymbol{u}}'\rangle_t(\boldsymbol{x}){:}\langle\tilde{\boldsymbol{u}}'\rangle_t(\boldsymbol{x}) + \mathrm{Tr}(\langle\boldsymbol{\tau}\rangle_t(\boldsymbol{x})))$, that necessitate Reynolds-averaged secondary cells, a mechanism first identified by Hinze (1967). Under this framework, a relative space-local excess in *tke* production necessitates entrainment of relatively low-*tke* fluid. In the present context, the relative excesses occur above the streamwise-aligned rows. For brevity, and because *tke* has been shown in complementary prior articles (Zheng & Anderson 2021), *tke* contours are not shown here. We have prepared targeted results of total streamwise–wall-normal turbulent stress, which is indicative of *tke* in rough wall channel turbulence.

For the d-type cases wherein the flow skims across the elements and the roughness sublayer depth is elevated, as per figure 4(a,b), the region of low-*tke* fluid resides between the adjacent rows of trees, thereby requiring lateral entrainment. For reference, note that the roughness sublayer is defined here as the region over which element-driven upwelling occurs (Goldstein & Tuan 1998). For the k-type cases, in contrast, vortical mixing between successive streamwise-aligned trees and penetration of the canopy enables a relatively smaller roughness sublayer. As such, low-*tke* fluid resides aloft, enabling downwelling (discussion to follow).

To further the discussion, figure 5 shows vertical profiles of vertical velocity for all table 1 cases, with the exception of the benchmark comparison cases, where panels (a–d) show profiles for cases $d1i$, $d2i$, $k3i$ and $k4i$, respectively. The profiles are recovered from a spanwise location coincident with the centre of a row of elements, and downwelling and upwelling annotations are provided for perspective.

For the d-type cases (figure 5a,b), the magnitude of the vertical gradient of vertical velocity increases monotonically with increasing δ_2; in addition, apparent depth of the roughness sublayer thickens with increasing δ_2, which is consistent with growth of the roughness sublayer vortices with growing δ_2 (Yang & Anderson 2017*b*; Anderson *et al.* 2018). This pattern of upwelling aloft the elements occurs for both d-type cases; for the k-type cases: the vertical gradients of vertical velocity are significantly smaller by virtue of the larger streamwise distances between successive elements. This is evidence of the aforementioned 'lowering' of the roughness sublayer to occupy the canopy: the intensity of canopy-driven mixing and associated upwelling from canopy elements declines monotonically from the d- to k-type cases. Note also that for the k-type cases

https://doi.org/10.1017/jfm.2022.583 Published online by Cambridge University Press

the regions of downwelling emerge for cases with larger spanwise heterogeneity (darker profiles). This is consistent with aforementioned secondary flow polarity reversal as topographic attributes vary.

In seminal work, Reynolds-averaged secondary flows due to spatial heterogeneity of turbulent stresses, so-called Prandtl's secondary flow of the second kind, were first interpreted via the balance of *tke* (Hinze 1967) (for a review, see Bradshaw 1987 and references therein). In the context of hydraulic flows over beds with spanwise-variable hydrodynamic roughness, Vermaas *et al.* (2011) adopted the arguments of Hinze (1967) to interpret secondary flow polarity (Wang & Cheng 2005). More recently, Anderson *et al.* (2015*a*) adopted the framework set forth by Hinze (1967) to explain secondary flow attributes in high-Reynolds-number rough-wall boundary layers and channels. Prandtl's secondary flow of the second kind can be readily understood via the Reynolds-averaged *tke* balance:

$$\langle \tilde{v} \rangle_{1t} \partial_y tke + \langle \tilde{w} \rangle_{1t} \partial_z tke = \mathcal{P} - \epsilon, \tag{3.1}$$

where the first and second terms on the right-hand side are production and dissipation, respectively. Application of (3.1) over a vertical profile at a spanwise transect coincident with a row of trees, the first left-hand side term vanishes. Recall that $\mathcal{P} = \langle \boldsymbol{u}' \otimes \boldsymbol{u}' \rangle_{xt} : \boldsymbol{\nabla} \langle \boldsymbol{u} \rangle_{xt}$, where $\boldsymbol{u}' = \boldsymbol{u} - \langle \boldsymbol{u} \rangle_{xt}$ and where $\boldsymbol{T} = \boldsymbol{u}' \otimes \boldsymbol{u}'$ is the Reynolds (total) stress tensor (in the LES context, recovered via addition of the resolved and subgrid-scale stresses). It is self-evident that for the present channel flows, $\boldsymbol{u}' \otimes \boldsymbol{u}'$ is dominated by the streamwise–wall-normal component whereas $\boldsymbol{\nabla} \langle \boldsymbol{u} \rangle_{xt}$ is dominated by the wall-normal gradient of streamwise velocity, i.e. $\mathcal{P} \approx \langle T_{xz} \rangle_{xt} \partial_z \langle u \rangle_{xt}$. Above the elements, intense shear leads production of *tke* to exceed dissipation, automatically imposing $\mathcal{P} - \epsilon > 0$. Irrespective of the magnitude of *tke* above the elements, the vertical gradient of *tke* must be negative, subsequently necessitating downwelling in order to match the polarity of the left- and right-hand side. It is emphasised that this framework has been used rigorously in prior, complementary studies (Wang & Cheng 2005; Vermaas *et al.* 2011; Anderson *et al.* 2015*a*; Salesky, Calaf & Anderson 2022). For this reason, we have not repeated the exercise here, and rather have used qualitative attributes of the *tke* balance to establish context for the observations. Note also that other researchers have considered how imbalances in production and dissipation aloft flows over horizontally homogeneous canopies affect the hierarchy of dynamically active scales present and associated normalising length scales (Pan & Chamecki 2016; Ghannam *et al.* 2018).

Figure 6 shows contours of total streamwise–wall-normal stresses, $\langle T_{xz} \rangle_{xt} / u_*^2$, for the same cases highlighted in figure 4, where δ_1 and δ_2 increases in the left-to-right and top-to-bottom directions, respectively; recall that $u_*^2 = \max \langle |\tilde{u}' \tilde{w}'| \rangle_t (\boldsymbol{x}) + \max \langle |\tau_{xz}| \rangle_t (\boldsymbol{x})$ (Bailey & Stoll 2013). Note that for the figure 4 cases that exhibited upwelling, *d*-type cases with smallest δ_2, we see corresponding δ-scale plumes of elevated T_{xz} throughout the domain (figure 6*a*,*b*). In contrast, for cases with established downwelling aloft the elements, the plume of elevated T_{xz} resides within the canopy. When viewed through the framework established by Hinze (1967), the *d*-type modality (figures 6*a*,*b*) can be understood as inducing a region of elevated $\mathcal{P}$ that is so large that entrainment from aloft is not possible; instead, *tke* can be optimally balanced via lateral entrainment. In contrast, when the roughness sublayer occupies the canopy, as it does for the *k*-type response, the region of elevated T_{xz} is relatively smaller. With this, regions of elevated $\mathcal{P}$ are confined to the canopy, providing greater spatial extent for entrainment of low-*tke* fluid from aloft (discussion to follow).

To provide more clarity on figure 6 and accompanying discussion, in figure 7 we show vertical profiles of $\langle T_{xz} \rangle_{xt} (y_l, z)$, where y_l is a spanwise location coincident with

https://doi.org/10.1017/jfm.2022.583 Published online by Cambridge University Press

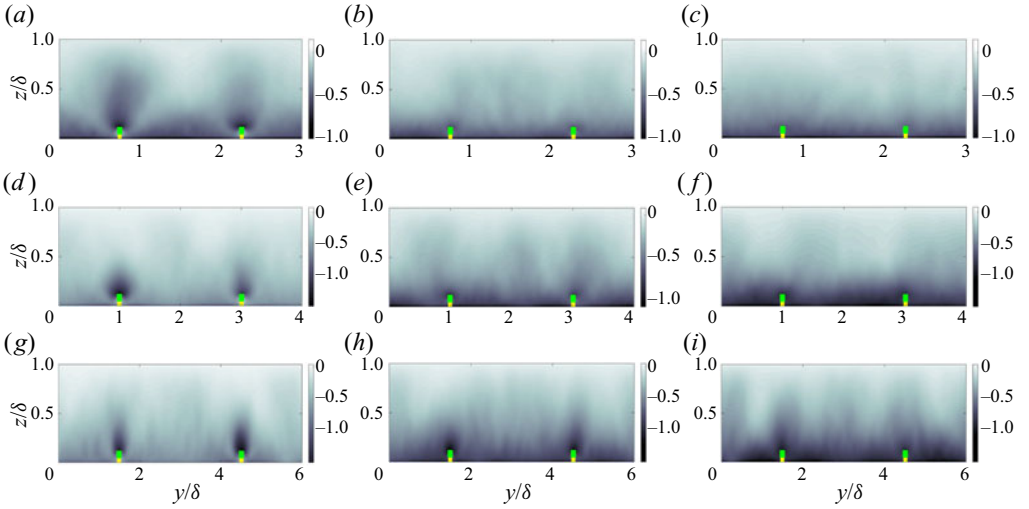


Figure 6. Contours of x- and Reynolds-averaged streamwise–wall-normal Reynolds (turbulent) stresses, $\langle T_{xz}\rangle_{xt}/u_*^2 = (\langle\tilde{u}'\tilde{w}'\rangle_{xt} + \langle\tau_{xz}\rangle_{xt})/u_*^2$, in the y–z plane. Results are shown for table 1 cases with $\delta_2/\delta = 1.5$ (a–c shows results for cases $d17$, $k37$ and $k47$), 2 (d–f shows results for cases $d18$, $k38$ and $k48$) and 3 (g–i shows results for cases $d19$, $k39$ and $k49$) and streamwise spacing $\delta_1/h = 0.25$ (a,d,g), 5.75 (b,e,hs) and 11.75 (c,f,i). Canopy elements are denoted with green silhouettes.

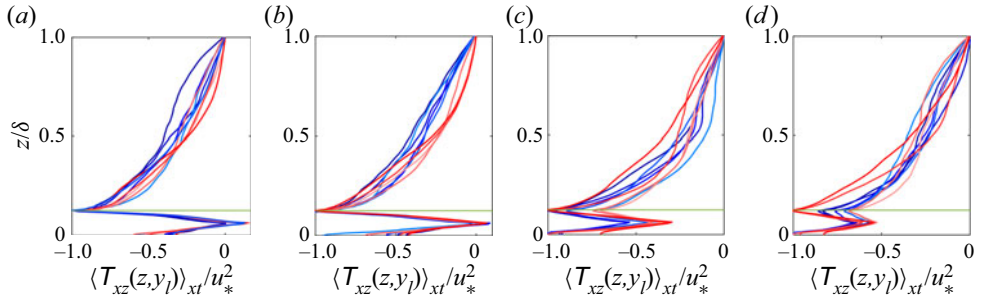


Figure 7. Vertical profiles of x- and Reynolds-averaged streamwise–wall-normal Reynolds (turbulent) stresses, $\langle T_{xz}\rangle_{xt} = \langle\tilde{u}'\tilde{w}'\rangle_{xt} + \langle\tau_{xz}\rangle_{xt}$, at spanwise location, y_l, coincident with the centre of a row of trees. Panels (a–d) show results for cases $d1i$, $d2i$, $k3i$ and $k4i$, respectively, where $i = 1$ to 9 corresponds with a colour transition from blue to red. The canopy elevation, h/δ, is denoted by horizontal green lines.

the centreline of a row of trees. As per figure 5, a horizontal green profile has been superimposed to denote the elevation of the canopy. For the d-type cases, as might be expected, the shear layer is most intense at h/δ (figure 7a,b); in contrast, for the k-type cases, elevated shear occurs throughout the canopy, and generally attains its maximum value at the wall, indicative of declining fluxes of momentum to the canopy with increasing δ_1.

Note that because the profiles are shown at a discrete spanwise location, there is no means to incorporate the dispersive stress component, that is, stresses due to spatial heterogeneity of the mean flow, as per Calaf, Meneveau & Meyers (2010) or Bailey & Stoll (2013). In separate work, we have computed vertical profiles of the plane-averaged stresses, which recovered the expected linearly decreasing profile. The profiles observed in figure 7 are a consequence of flow response to the canopy attributes.

https://doi.org/10.1017/jfm.2022.583 Published online by Cambridge University Press

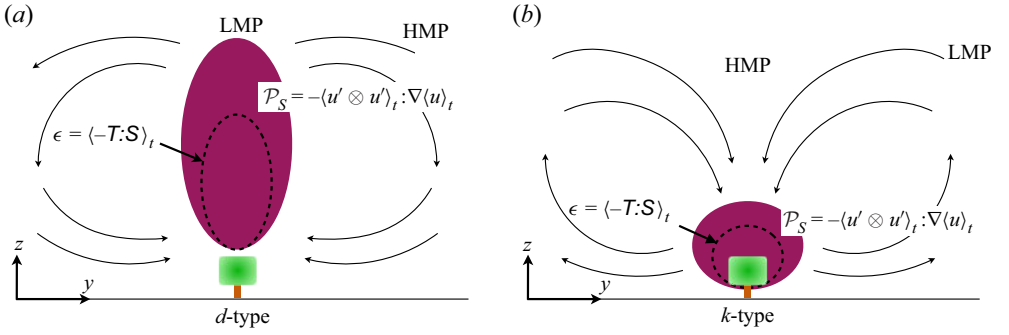


Figure 8. Idealised depiction of *tke* production and dissipation dynamics for the *d*- (*a*) and *k*-type cases (*b*), respectively. Red regions denote locations of elevated production, dashed grey denotes regions of elevated dissipation.

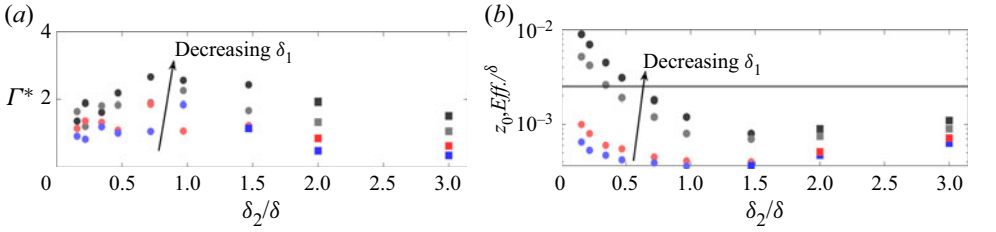


Figure 9. Bulk flow attributes for table 1 simulations. Panels (*a*,*b*) show compensated circulation, Γ^* (3.2) and effective roughness length, $z_{0,Eff.}/\delta$, respectively, shown against spanwise heterogeneity, δ_2/δ. Symbols correspond with $\delta_1/h = 0.25$ (black symbols), 1 (grey symbols), 5.75 (red symbols) and 11.75 (blue symbols); direction of decreasing δ_1 superimposed for perspective. Cases with upwelling and downwelling above a row of elements are denoted with filled circles and filled squares, respectively. In panel (*b*), the horizontal solid line shows base roughness length, $\hat{z}_0/\delta$.

Figure 8 is an illustrative depiction of the aforementioned *tke* balance mechanisms responsible for the observed secondary flow polarity reported in figures 3 and 4. For the *d*-type cases, the relatively small values of δ_1 prevent the canopy-driven shear layer from occupying the canopy, and instead production of turbulence occurs over the depth of the flow (figure 8*a*). This precludes entrainment of low-*tke* fluid from aloft, thereby necessitating lateral entrainment. This explains the observed low-momentum pathway above the elements for *d*-type cases (Barros & Christensen 2014). For the *k*-type cases, regions of elevated *tke* production occupies the canopy (figure 8*b*), which enables lateral entrainment from aloft and formation of HMPs above the elements.

To conclude the present discussion, figure 9(*a*) presents datapoints for compensated circulation:

$$\Gamma^* = \frac{\Gamma}{u_* \delta} = \int_{d^2\boldsymbol{x}} |\langle \tilde{\omega}_x \rangle_{xt}(y, z)| \, \mathrm{d}y \, \mathrm{d}z, \tag{3.2}$$

as per Yang & Anderson (2017*b*), and figure 9(*b*) presents datapoints for *a posteriori*-recovered effective roughness length, $z_{0,Eff.}/\delta$. Each datapoint corresponds with a table 1 simulation, as per the caption, with the notable exception of the benchmark comparison cases, which are utilised in the Appendix.

Compensated circulation is a helpful bulk metric for quantifying intensity of roughness-driven secondary flows; in the absence of spanwise heterogeneity, or for infinite

https://doi.org/10.1017/jfm.2022.583 Published online by Cambridge University Press

spanwise heterogeneity, $\Gamma^* = 0$. Between these limiting values of δ_2, Γ^* varies, where interested readers may consult Yang & Anderson (2017*b*) or Anderson *et al.* (2018) for further discussion.

In figure 9(*a*), the datapoints exhibit non-monotonic dependence on δ_2, which has been reported in numerous preceding articles (Yang & Anderson 2017*b*; Anderson *et al.* 2018); it is noted that Medjnoun *et al.* (2018) have also qualitatively defined this with their 'significance' parameter. These trends can be interpreted as growing secondary flow intensity in the roughness regime (recall figure 1*c*), as the element-driven secondary flows in the *d*-type regime grow in spatial extent with increasing δ_2. This trend asymptotes in the transitional regime, before reversing trend. This is a consequence of the secondary cells occupying a relatively lesser spatial extent, and with the emergence of HMPs and their relatively lower streamwise vorticity (figure 8 and accompanying text). The symbol colour codes denote the respective values of δ_1, and the direction of decreasing δ_1 is superimposed, for perspective.

As might be anticipated, as δ_1 decreases, the topography becomes relatively 'more rough' and the element-driven secondary cells exhibit more intense compensated circulation. This trend, and the asymptotic turning point for $\delta_2/\delta \approx 1$, is invariant to *d*- or *k*-type values. Note that on figure 9(*a*), filled circles and filled squares correspond with cases that exhibit Reynolds-averaged upwelling or downwelling, respectively. Recall that the latter, downwelling aloft the elements, corresponds with antecedent observations of HMPs reported by Christensen, Anderson, and others (i.e. Willingham *et al.* 2013; Barros & Christensen 2014; Anderson *et al.* 2015*a*). Detailed inspection of figure 9(*a*) reveals that secondary flow polarity reverses for the *k*-type cases first (blue square at $\delta_2/\delta \approx 1.5$), whereas all cases reverse for larger δ_2/δ. This is evidence of the aforementioned polarity reversal for larger δ_1, as the production–dissipation imbalance occupies the canopy.

Figure 9(*b*) shows effective roughness length normalised by flow depth, $z_{0,Eff.}/\delta$, which is recovered *a posteriori* via least-squares fit of a logarithmic (equilibrium) profile to vertical profiles of plane- and time-averaged streamwise velocity, $\langle\tilde{u}\rangle_{xyt}/u_*$. The least-squares fit is based on data over the range, $0.4 \leq z/\delta \leq 0.8$. Given that the effective roughness lengths are based on a rigorous least-squares fit, and the strong trends observed on the panels, the reported values of $z_{0,Eff.}$ may be regarded as robust and accurate. To provide support for these results, please note that figure 10 shows vertical profiles for plane- and time-averaged streamwise velocity. For all cases, it is clear that a well-established logarithmic region is present, evidenced by comparison against the superimposed idealised profile. For perspective, the elevation of the canopy elements is superimposed; an idealised logarithmic profile (thick black) is superimposed, which illustrates that the aforementioned protocol for recovery of $z_{0,Eff.}$ is efficacious.

On figure 9(*b*), the direction of decreasing δ_1 is superimposed, for context, and as expected the roughness length increases monotonically with decreasing δ_1. This can be understood as a direct consequence of additional drag associated with larger leaf area index (recall also figure 2). Similarly, for the roughness-regime cases (*d*- and *k*-type), effective roughness decreases monotonically as spanwise spacing increases and leaf area index declines. This trend reverses for transitional cases and tends toward increasing roughness for yet-larger δ_2. Recall, however, that it is these cases for which the distinct HMPs emerge and persistent downwelling occurs above the elements due to the production–dissipation imbalance and entrainment of low-*tke* fluid. Thus, the entrainment of relatively high-momentum fluid from aloft manifests as an added drag. It is noted, also, that the onset of this is reported for the largest δ_1 case, when the associated roughness sublayer occupies the greatest spatial extent of the canopy. On figure 9(*b*), the base

https://doi.org/10.1017/jfm.2022.583 Published online by Cambridge University Press

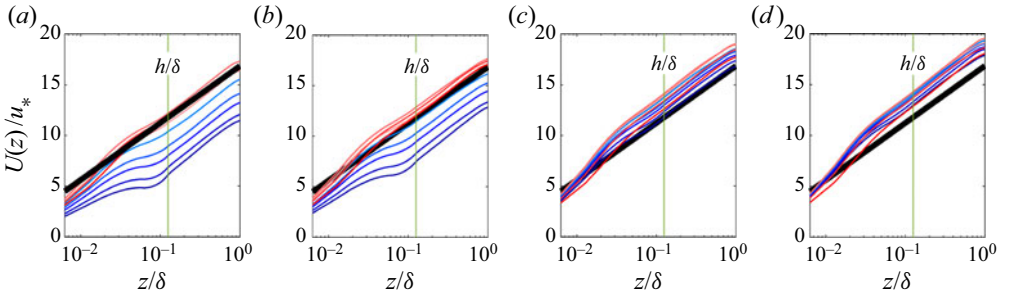


Figure 10. Vertical profiles of plane- and Reynolds-averaged streamwise velocity, $U(z) = \langle\tilde{u}\rangle_{xyt}(z)$. Panels (*a–d*) show results for cases *d*1*i*, *d*2*i*, *k*3*i* and *k*4*i*, respectively, where $i = 1$–9 corresponds with a colour transition from red to blue. The canopy elevation, h/δ, is denoted by vertical green line and annotation. An idealised logarithmic profile based on roughness length, $z_0/\delta = 10^{-3}$, is superimposed for perspective.

roughness, $\hat{z}_0/\delta$, prescribed in the LES (alongside the bluff canopy elements; § 2.1) is shown via horizontal black line. As expected, as δ_2 increases, noting that the limit, $\delta_2 = \infty$, corresponds with a homogeneous roughness length, $\hat{z}_0$, we see tendency towards $\hat{z}_0$.

3.1. *k- and d-type roughness, flow response*

The results in figure 9(*b*) can be interpreted somewhat differently by quantifying the correlation between effective roughness length and corresponding canopy attributes. One such correlation, which has received widespread use over many years (Garratt 1994; Zagarola & Smits 1998) is:

$$z_{0,Eff.}(h, \delta_1, \delta_2) \sim \sigma_h = \alpha(\delta_1, \delta_2)\sigma_h + \hat{z}_0, \tag{3.3}$$

where α is a proportionality constant relating height r.m.s., $\sigma_h = (\langle h^2\rangle_{xy} - \langle h\rangle_{xy}^2)^{1/2}$, and roughness length, and $\hat{z}_0$ is the aforementioned 'baseline' roughness length (Anderson & Meneveau 2010*b*). Figure 11(*a*) shows a contour flood of σ_h for the table 1 cases, with the exception of the benchmark comparison cases. As might be expected, the largest values occur for the smallest δ_1 and δ_2, and σ_h decreases monotonically with increases in both.

Figure 11(*b*) shows the corresponding contour flood of z_0/δ for the table 1 cases, where the idealised regimes depicted on figure 1(*a*) are superimposed for context. The elevated roughness contours for small δ_1 and δ_2 were already presented and discuss in figure 9(*b*), likewise the trend reversal and elevated values for small large δ_2 and small δ_1, as the secondary cells reverse and high momentum fluid is entrained toward the roughness elements. However, the contour of $\alpha(\delta_1, \delta_2)$ (figure 11*c*) provides detailed illustration of the roughness length and height r.m.s. correlate. Note that the minimal value required to correlate z_0 and σ_h *a priori* manifests as a channel spanning cases with the smallest δ_2 and largest δ_1 to cases with the smallest δ_1 and transitional δ_2. The proportionality constant, $\alpha(\delta_1, \delta_2)$, was recovered via rearrangement of (3.3).

Cases with small δ_2 and large δ_1 correspond with *k*-type arrangements, with spanwise spacing *k*-type cases, with spanwise spacing sufficiently small that vigorous mixing occurs within the canopy and the elements absorb the greatest fraction of the momentum flux; for smaller δ_1, mixing within the canopy is attenuated and the relative efficiency of the correlation declines. As δ_2 increases, thereby providing greater spatial extent within the canopy, and as δ_1 decreases, element-driven mixing occupies the spatial 'gaps' between the

https://doi.org/10.1017/jfm.2022.583 Published online by Cambridge University Press

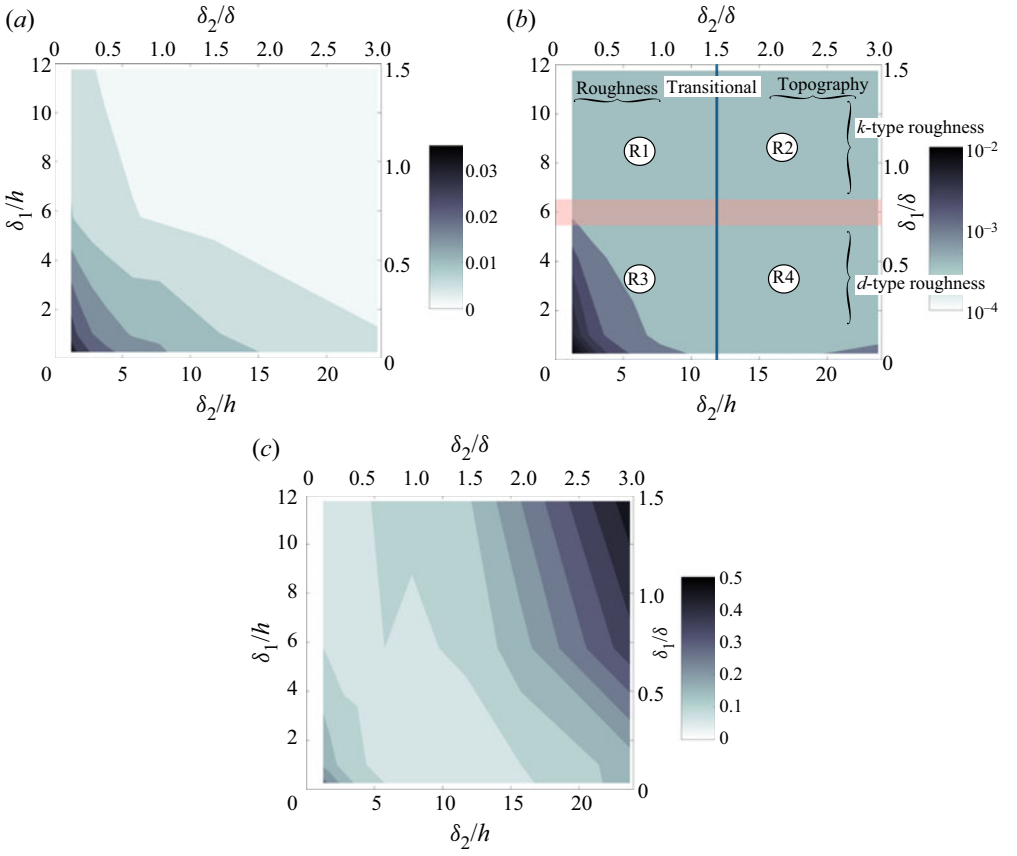


Figure 11. Large-scale aerodynamic response to variable canopy attributes. Panels (*a–c*) show height r.m.s., $\sigma_h = (\langle h^2 \rangle_{xy} - \langle h \rangle_{xy}^2)^{1/2}$, *a posteriori*-recovered effective roughness length, $z_{0,Eff.}$, and (3.3) proportionality constant, α, respectively (note that individual values for σ_h, $z_{0,Eff.}$ and α are recorded in table 1). Panel (*b*) illustrates how the confluence of variable δ_1 and δ_2 preclude automatic surface regime description. Nominal regions where δ_2 renders the surface a 'roughness' or 'topography' are shown (top and bottom abscissa) against regions where δ_1 renders the surface *k*- or *d*-type (left and right ordinate), where δ_1 and δ_2 are defined with respect to flow depth and canopy height, for perspective. This confluence yields quadrant regions R1, R2, R3 and R4, which are graphically illustrated in figure 1(*c*).

streamwise-aligned row of elements. It is only for this relatively narrow range of the δ_1–δ_2 parameter space that vigorous mixing within the canopy corresponds with the smallest values of α, and values of α closest to prior studies (Zagarola & Smits 1998; Anderson & Meneveau 2011).

4. Conclusion

LES has been used to perform an assessment of turbulent channel flow response to rough canopies composed of virtual trees. The arrangements are carefully assembled to isolate flow response with variable streamwise and spanwise spacing, the former affecting *d*- or *k*-type response, the latter affecting roughness, transition or topography response; no prior article has simultaneously addressed the role of both parameters. Consistent with prior articles, we find that for $\delta_2/\delta \lesssim 1$ (in the roughness regime), upwelling is persistent above the elements irrespective of the presence of a *d*- or *k*-type arrangement. However, in

https://doi.org/10.1017/jfm.2022.583 Published online by Cambridge University Press

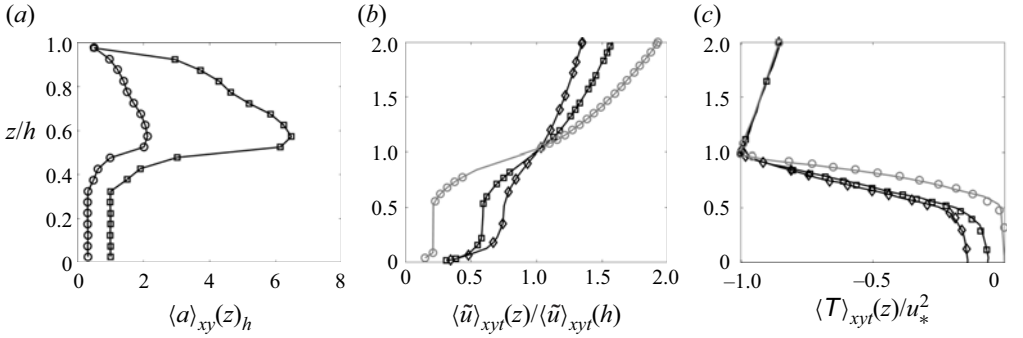


Figure 12. Canopy attributes and resultant Reynolds-averaged flow statistics for cases R1.6, R3.1 and R3.6 (salient case details summarised in table 1; cases adopted from Bailey & Stoll 2013). Panel (*a*) shows vertical profiles of leaf-area density; panels (*b*,*c*) show vertical profiles of plane- and time-averaged streamwise velocity and streamwise–wall-normal turbulent stresses, respectively. Solid lines show results from LES, whereas symbols show datapoints recovered from Bailey & Stoll (2013), where light grey, grey and black lines/symbols correspond with cases R3.1, R3.6 and R1.6, respectively.

the transitional regime, δ_1 regulates the onset of secondary flow polarity reversal and the emergence of established HMPs. For the asymptotic inertial conditions addressed herein, roughness element attributes are not expected to significantly alter the results, although subsequent work may well be needed to resolve this issue.

Funding. This work was supported by the National Science Foundation (grant no. AGS-1839929). Computational resources were provided by the Texas Advanced Computer Center at the University of Texas.

Declaration of interests. The authors report no conflict of interest.

Author ORCIDs.
W. Anderson https://orcid.org/0000-0002-5058-9672.

Appendix. Comparison against benchmark datasets

In order to demonstrate efficacy of the LES code used for this article, we repeated the simulations first carried out by Bailey & Stoll (2013). Attributes for these cases are summarised in table 1 (R1.6, R3.1 and R3.6). For brevity, we show only targeted results here, which are shown in figure 12, where panel (*a*) shows vertical profiles of plane-averaged LAI, whereas panels (*b*,*c*) show plane- and time-averaged streamwise velocity and streamwise–wall-normal turbulent stresses. Figure 12(*a*) indicates that the cases have been correctly replicated; panels (*b*,*c*) illustrate agreement with the prior dataset, at least to the second order. These results provide support for results and accompanying scientific deductions presented throughout the main text.

References

Anderson, W. 2012 An immersed boundary method wall model for high-Reynolds number channel flow over complex topography. *Intl J. Numer. Meth. Fluids* **71**, 1588–1608.

Anderson, W. 2019 Non-periodic phase-space trajectories of roughness-driven secondary flows in high-Re_τ boundary layers and channels. *J. Fluid Mech.* **869**, 27–84.

Anderson, W., Barros, J.M., Christensen, K.T. & Awasthi, A. 2015*a* Numerical and experimental study of mechanisms responsible for turbulent secondary flows in boundary layer flows over spanwise heterogeneous roughness. *J. Fluid Mech.* **768**, 316–347.

https://doi.org/10.1017/jfm.2022.583 Published online by Cambridge University Press

ANDERSON, W., LI, Q. & BOU-ZEID, E. 2015*b* Numerical simulation of flow over urban-like topographies and evaluation of turbulence temporal attributes. *J. Turbul.* **16**, 809–831.
ANDERSON, W. & MENEVEAU, C. 2010*a* A large-eddy simulation model for boundary-layer flow over surfaces with horizontally resolved but vertically unresolved roughness elements. *Boundary-Layer Meteorol.* **137**, 397–415.
ANDERSON, W. & MENEVEAU, C. 2010*b* A large-eddy simulation model for boundary-layer flow over surfaces with horizontally resolved but vertically unresolved roughness elements. *Boundary-Layer Meteorol.* **137**, 397–415.
ANDERSON, W. & MENEVEAU, C. 2011 A dynamic large-eddy simulation model for boundary layer flow over multiscale, fractal-like surfaces. *J. Fluid Mech.* **679**, 288–314.
ANDERSON, W., YANG, J., SHRESTHA, K. & AWASTHI, A. 2018 Turbulent secondary flows in wall turbulence: vortex forcing, scaling arguments, and similarity solution. *Environ. Fluid Mech.* **18**, 1351–1378.
ANTONIA, R.A. & LUXTON, R.E. 1971 The response of a turbulent boundary layer to a step change in surface roughness. Part I. Smooth to rough. *J. Fluid Mech.* **48**, 721–761.
AWASTHI, A. & ANDERSON, W. 2018 Numerical study of turbulent channel flow perturbed by spanwise topographic heterogeneity: amplitude and frequency modulation within low-and high-momentum pathways. *Phys. Rev. Fluids* **3**, 044602.
BAI, K., KATZ, J. & MENEVEAU, C. 2015 Turbulent flow structure inside a canopy with complex multi-scale elements. *Boundary-Layer Meteorol.* **155**, 435–457.
BAILEY, B.N. & STOLL, R. 2013 Turbulence in sparse, organized vegetative canopies: a large-eddy simulation study. *Boundary-Layer Meteorol.* **147**, 369–400.
BAILEY, B.N. & STOLL, R. 2016 The creation and evolution of coherent structures in plant canopy flows and their role in turbulent transport. *J. Fluid Mech.* **789**, 425–460.
BAILEY, B.N., STOLL, R., PARDYJAK, E.R. & MAHAFFEE, W.F. 2014 Effect of vegetative canopy architecture on vertical transport of massless particles. *Atmos. Environ.* **95**, 480–489.
BARROS, J.M. & CHRISTENSEN, K.T. 2014 Observations of turbulent secondary flows in a rough-wall boundary layer. *J. Fluid Mech.* **748**, R1.
BELCHER, S.E., HARMAN, I.N. & FINNIGAN, J.J. 2012 The wind in the willows: flows in forest canopies in complex terrain. *Annu. Rev. Fluid Mech.* **44**, 479–504.
BELCHER, S.E., JERRAM, N. & HUNT, J.C.R. 2003 Adjustment of a turbulent boundary layer to a canopy of roughness elements. *J. Fluid Mech.* **488**, 369–398.
BOU-ZEID, E., ANDERSON, W., KATUL, G.G. & MAHRT, L. 2020 The persistent challenge of surface heterogeneity in boundary-layer meteorology: a review. *Boundary-Layer Meteorol.* **177**, 227–245.
BOU-ZEID, E., MENEVEAU, C. & PARLANGE, M.B. 2005 A scale-dependent Lagrangian dynamic model for large eddy simulation of complex turbulent flows. *Phys. Fluids* **17**, 025105.
BRADSHAW, P. 1987 Turbulent secondary flows. *Annu. Rev. Fluid Mech.* **19**, 53–74.
BRADSHAW, P. 2003 Turbulent secondary flows. *Annu. Rev. Fluid Mech.* **19**, 53–74.
BROWN, A.R., HOBSON, J.M. & WOOD, N. 2001 Large-eddy simulation of neutral turbulent flow over rough sinusoidal ridges. *Boundary-Layer Meteorol.* **98**, 411–441.
BRUNDRETT, E. & BAINES, W.D. 1964 The production and diffusion of vorticity in duct flow. *J. Fluid Mech.* **19** (3), 375–394.
CALAF, M., MENEVEAU, C. & MEYERS, J. 2010 Large eddy simulation study of fully developed wind-turbine array boundary layers. *Phys. Fluids* **22**, 015110.
CASTRO, I.P. 2007 Rough-wall boundary layers: mean flow universality. *J. Fluid Mech.* **585**, 469–485.
CHUNG, D., HUTCHINS, N., SCHULTZ, M.P. & FLACK, K.A. 2021 Predicting the drag of rough surfaces. *Annu. Rev. Fluid Mech.* **53**, 439–471.
FINNIGAN, J. 2000 Turbulence in plant canopies. *Annu. Rev. Fluid Mech.* **32**, 519–571.
FINNIGAN, J.J., SHAW, R.H. & PATTON, E.G. 2009 Turbulence structure above a vegetation canopy. *J. Fluid Mech.* **637**, 387–424.
FLACK, K.A. & SCHULTZ, M.P. 2010 Review of hydraulic roughness scales in the fully rough regime. *Trans. ASME J. Fluids Engng* **132** (4), 041203.
FLACK, K.A., SCHULTZ, M.P. & CONNELLY, J.S. 2007 Examination of a critical roughness height for outer layer similarity. *Phys. Fluids* **19** (9), 095104.
GARRATT, J.R. 1994 *The Atmospheric Boundary Layer*. Cambridge University Press.
GESSNER, F.B. 1973 The origin of secondary flow in turbulent flow along a corner. *J. Fluid Mech.* **58** (1), 1–25.
GHANNAM, K., KATUL, G.G., BOU-ZEID, E., GERKEN, T. & CHAMECKI, M. 2018 Scaling and similarity of the anisotropic coherent eddies in near-surface atmospheric turbulence. *J. Atmos. Sci.* **75**, 943–964.
GHISALBERTI, M. 2009 Obstructed shear flows: similarities across systems and scales. *J. Fluid Mech.* **641**, 51.

https://doi.org/10.1017/jfm.2022.583 Published online by Cambridge University Press

GOLDSTEIN, D.B. & TUAN, T.-C. 1998 Secondary flow induced by riblets. *J. Fluid Mech.* **363**, 115–151.
GRAHAM, J. & MENEVEAU, C. 2012 Modeling turbulent flow over fractal trees using renormalized numerical simulation: alternate formulations and numerical experiments. *Phys. Fluids* **24**, 125105.
GRASS, A.J. 1971 Structural features of turbulent flow over smooth and rough boundaries. *J. Fluid Mech.* **50**, 233.
HARMON, I. & FINNIGAN, J.J. 2007 A simple unified theory for flow in the canopy and roughness sublayer. *Boundary-Layer Meteorol.* **123**, 339–364.
HINZE, J.O. 1967 Secondary currents in wall turbulence. *Phys. Fluids* **10** (9), S122–S125.
HOAGLAND, L.C. 1960 Fully developed turbulent flow in straight rectangular ducts – secondary flow, its cause and effect on the primary flow. PhD thesis, Massachusetts Inst. of Tech.
HUTCHINS, N. & MARUSIC, I. 2007 Evidence of very long meandering features in the logarithmic region of turbulent boundary layers. *J. Fluid Mech.* **579**, 1–28.
JIMENEZ, J. 2004 Turbulent flows over rough walls. *Annu. Rev. Fluid Mech*. **36**, 173–196.
KEVIN, K., MONTY, J.P., BAI, H.L., PATHIKONDA, G., NUGROHO, B., BARROS, J.M., CHRISTENSEN, K.T. & HUTCHINS, N. 2017 Cross-stream stereoscopic particle image velocimetry of a modified turbulent boundary layer over directional surface pattern. *J. Fluid Mech.* **813**, 412–435.
MACDONALD, R., GRIFFITHS, R. & HALL, D. 1998 An improved method for the estimation of surface roughness of obstacle arrays. *Atmos. Environ.* **32**, 1857–1864.
MEDJNOUN, T., VANDERWEL, C. & GANAPATHISUBRAMANI, B. 2018 Characteristics of turbulent boundary layers over smooth surfaces with spanwise heterogeneities. *J. Fluid Mech.* **838**, 516–543.
MEDJNOUN, T., VANDERWEL, C. & GANAPATHISUBRAMANI, B. 2020 Effects of heterogeneous surface geometry on secondary flows in turbulent boundary layers. *J. Fluid Mech.* **886**, A31.
NUGROHO, B., HUTCHINS, N. & MONTY, J.P. 2013 Large-scale spanwise periodicity in a turbulent boundary layer induced by highly ordered and directional surface roughness. *Intl J. Heat Fluid Flow* **41**, 90–102.
PAN, Y. & CHAMECKI, M. 2016 A scaling law for the shear-production range of second-order structure functions. *J. Fluid Mech.* **801**, 459–474.
PATHIKONDA, G. & CHRISTENSEN, K.T. 2017 Inner-outer interactions in a turbulent boundary layer overlying complex roughness. *Phys. Rev. Fluids* **2**, 044603.
PERKINS, H.J. 1970 The formation of streamwise vorticity in turbulent flow. *J. Fluid Mech.* **44** (4), 721–740.
PERRY, A.E., SCHOFIELD, W.H. & JOUBERT, P. 1969 Rough wall turbulent boundary layers. *J. Fluid Mech.* **37**, 383–413.
PRANDTL, L. 1952 *Essentials of Fluid Dynamics*. Blackie and Son.
RAUPACH, M.R., ANTONIA, R.A. & RAJAGOPALAN, S. 1991 Rough-wall turbulent boundary layers. *Appl. Mech. Rev.* **44**, 1–25.
RAUPACH, M.R., FINNIGAN, J.J. & BRUNET, Y. 1996 Coherent eddies and turbulence in vegetation canopies: the mixing layer analogy. *Boundary-Layer Meteorol.* **78**, 351–382.
SALESKY, S.T., CALAF, M. & ANDERSON, W. 2022 Unstable turbulent channel flow response to spanwise-heterogeneous heat fluxes: Prandtl's secondary flow of the third kind. *J. Fluid Mech.* **934**, A46.
SHAW, R.H. & SCHUMANN, U. 1992 Large-eddy simulation of turbulent flow above and within a forest. *Boundary-Layer Meteorol.* **61**, 47–64.
STEVENS, R.J.A.M., WILCZEK, M. & MENEVEAU, C. 2014 Large-eddy simulation study of the logarithmic law for second- and higher-order moments in turbulent wall-bounded flow. *J. Fluid Mech.* **757**, 888–907.
STOLL, R., GIBBS, J.A., SALESKY, S.T., ANDERSON, W. & CALAF, M. 2020 Large-eddy simulation of the atmospheric boundary layer. *Boundary-Layer Meteorol.* **177**, 541–581.
STROH, A., SCHÄFER, K., FROHNAPFEL, B. & FOROOGHI, P. 2020 Rearrangement of secondary flow over spanwise heterogeneous roughness. *J. Fluid Mech.* **885**, R5.
SU, H.-B., SHAW, R.H., PAW, U.K.T., MOENG, C.-H. & SULLIVAN, P.P. 1998 Turbulent statistics of neutrally stratified flow within and above a sparse forest from large-eddy simulation and field observation. *Boundary-Layer Meteorol.* **88**, 367–397.
TOWNSEND, A.A. 1976 *The Structure of Turbulent Shear Flow*. Cambridge University Press.
VANDERWEL, C. & GANAPATHISUBRAMANI, B. 2015 Effects of spanwise spacing on large-scale secondary flows in rough-wall turbulent boundary layers. *J. Fluid Mech.* **774**, R2.
VERMAAS, D.A., UIJTTEWAAL, W.S.J. & HOITINK, A.J.F. 2011 Lateral transfer of streamwise momentum caused by a roughness transition across a shallow channel. *Water Resour. Res.* **47** (2), w02530.
WANG, Z.-Q. & CHENG, N.-S. 2005 Secondary flows over artificial bed strips. *Adv. Water Resour.* **28** (5), 441–450.
WILLINGHAM, D., ANDERSON, W., CHRISTENSEN, K.T. & BARROS, J. 2013 Turbulent boundary layer flow over transverse aerodynamic roughness transitions: induced mixing and flow characterization. *Phys. Fluids* **26**, 025111.

https://doi.org/10.1017/jfm.2022.583 Published online by Cambridge University Press

WYNGAARD, J.C. 2010 *Turbulence in the Atmosphere*. Cambridge University Press.
YANG, J. & ANDERSON, W. 2017*a* Numerical study of turbulent channel flow over surfaces with variable spanwise heterogeneities: topographically-driven secondary flows affect outer-layer similarity of turbulent length scales. *Flow Turbul. Combust.* **100**, 1–17.
YANG, J. & ANDERSON, W. 2017*b* Turbulent channel flow over surfaces with variable spanwise heterogeneity: establishing conditions for outer-layer similarity. *Flow Turbul. Combust.* **100**, 1–17.
YANG, X.I.A., SADIQUE, J., MITTAL, R. & MENEVEAU, C. 2016 Exponential roughness layer and analytical model for turbulent boundary layer flow over rectangular-prism roughness elements. *J. Fluid Mech.* **789**, 127–165.
ZAGAROLA, M.V. & SMITS, A.J. 1998 Mean-flow scaling of turbulent pipe flow. *J. Fluid Mech.* **373**, 33–79.
ZHENG, Y. & ANDERSON, W. 2021 Flow-roughness heterogeneity: critical obliquity and salient parameters. *J. Fluid Mech.* **913**, A12.

https://doi.org/10.1017/jfm.2022.583 Published online by Cambridge University Press